

OP34: The Zeeman effect

Andrei-Nicolae Taropa

April 10, 2024

Abstract

The Zeeman effect predicts splitting of atomic energy levels proportional to an applied magnetic field. Here we use a Fabry-Perot interferometer to measure changes caused by an external magnetic field in the fine structure of cadmium and mercury. The experiment verified the theoretical prediction by checking the effect of every quantum number on the Landé g factor and consequently on the individual energy level. Additionally, the experiment investigated the type of polarised light emitted, identified the handedness of the circularly polarised light, and measured the relative intensities of the spectral lines, therefore confirming the selection rules that arise from a quantum-mechanical treatment of the phenomenon. The experimental results were in agreement with the theory and there were no higher order perturbations, unaccounted for by the Zeeman effect, observable with the resolution achieved by this setup.

1 Introduction

Transitions of the electrons between the different atomic energy levels create the specific atomic spectra. When introduced in a magnetic field, some of the spectral lines split into multiple components. The splitting of quantum mechanical energy levels in a weak magnetic field is best described by the Zeeman effect. In the semi-classical Bohr model for the atom, the interaction of the magnetic moment μ_B caused by the orbital motion of the electron with the external field B leads to a simple energy level splitting $\pm\mu_BB$ (the *normal* Zeeman effect). However, this model does not include the spin magnetic moment and therefore it only correctly predicts energy level splitting when the total spin is 0. A quantum-mechanical model of an atom incorporating the spin magnetic moment m_s predicts an energy split of $m_s g_L \mu_B B$, where g_L is the Landé g factor. Historically this phenomenon was called the *anomalous* Zeeman effect, because the spin interaction can not be explained classically. The anomalous Zeeman effect predicts an energy dependence on the quantum numbers j , l , and s , for total angular momentum, orbital angular momentum and spin respectively, as verified in this report.

Our experiments observed the normal Zeeman effect using the red (644 nm) transition line of a cadmium lamp. The anomalous Zeeman effect was investigated in the cadmium green (509 nm) transition line. A mercury lamp was utilised to observe the green (546 nm) and the blue (435 nm) transition lines. The lines were observed in two configurations: perpendicular to the magnetic field (both the π and σ polarisation is visible) and along the field lines (only σ polarisation is visible). These measurements can fully verify the dependence of the splitting on spin, orbital angular momentum and total angular momentum.

In this paper we first discuss the theory behind the Zeeman effect (section 2.1), the experimental setup (section 2.2) and the methods used to measure the energy level splitting (section 2.4). Section 3 presents the results we obtained and how they are in agreement with the established theory. We include a detailed discussion of the measurement uncertainties and assumptions made during the data analysis (section 4) and end with the a summary of our results and future applications (section 5).

2 Theory and Methods

2.1 Energy levels and allowed transitions

One can find energy levels of an atom by considering the following Hamiltonian:

$$H = H_{CF} + H_{RE} + H_{SO} + H_{ZE} \quad (1)$$

where H_{CF} is the interaction with the central field, giving the gross structure of the energy levels, H_{RE} is the residual electrostatic perturbation, H_{SO} is the spin-orbit interaction perturbation and H_{ZE} is the interaction with an external magnetic field. In the weak field limit $H_{ZE} \ll H_{SO} \ll H_{RE}$ we can treat the Zeeman interaction H_{ZE} as a perturbation to the fine-structure levels that arise from L-S coupling [BS15]. The energy of the H_{ZE} interaction comes from the precessional motion of the orbital and spin magnetic moments around the external field:

$$H_{ZE} = \mu_B B \cdot (g_L L + g_S S) \quad (2)$$

where $g_L = 1$ and $g_S = 2$ are the g-factors for the orbit and spin respectively. $|nljm_L\rangle$ is the natural basis for the perturbation because it diagonalises the Hamiltonian H_{ZE} [Foo05]. This is because in order to calculate the energy perturbation of the energy level ΔE_{ZE} one needs to take the time average of the operators in equation (2). $L \cdot B$ and $S \cdot B$ are not constants of motion, but $J \cdot B$ is. We consider projections of L and S along J :

$$H_{ZE} = \mu_B B \cdot J(g_L \frac{|L \cdot J|}{|J|^2} + g_S \frac{|S \cdot J|}{|J|^2}) \quad (3)$$

We cast the equation into the form (4), where the Landé g factor is (5):

$$\Delta E_{ZE} = m_J g_L \mu_B B \quad (4)$$

The splitting is a function of the j , l , and s quantum numbers:

$$g_L = 1 + \frac{j(j+1) - l(l+1) + s(s+1)}{j(j+1)} \quad (5)$$

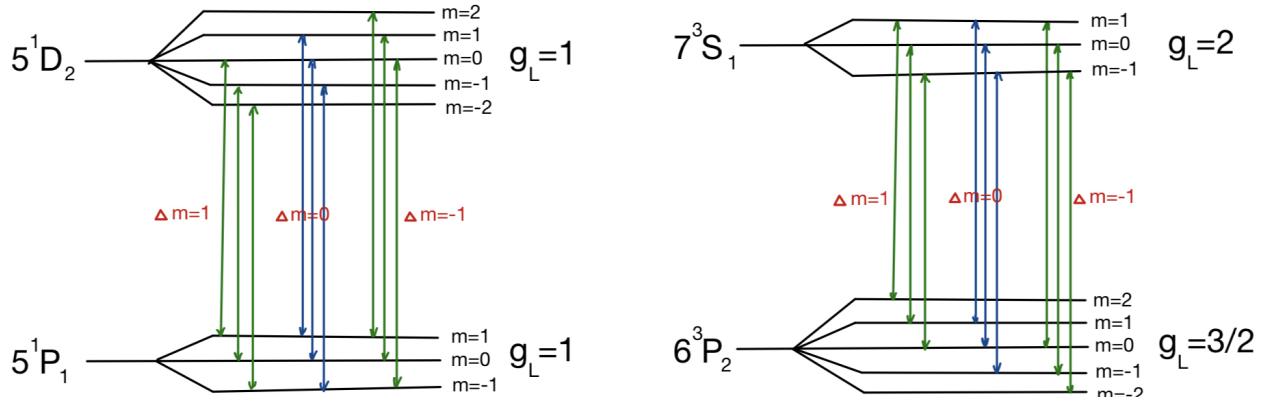


Figure 1: Schematic diagram of the Zeeman splitting. **Left side:** normal Zeeman effect in the Cadmium red line. The Landé g factors $g_L = 1$ for Cadmium, thus the line splits into 3 components. **Right side:** anomalous Zeeman effect in the Mercury green line. The splitting is identical to the Cadmium green line splitting. The Landé g factors g_L for Mercury are 2 and $3/2$, thus the line splits into 9 components.

The energy difference E between the two levels of the transition can be written neatly in the form of equation (6), by grouping the m_J and g_L factors of the individual levels into an effective g-factor. For a transition $2 \rightarrow 1$ the effective Landé g-factor is given by equation (7):

$$E = g_{eff} B \mu_B \quad (6)$$

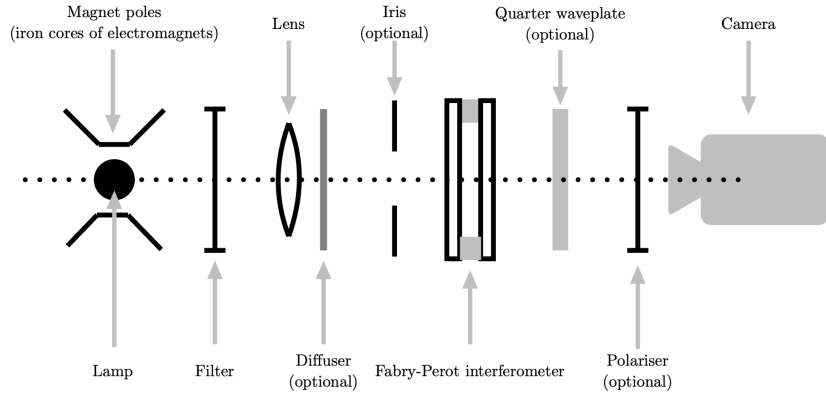


Figure 2: Diagram of the experimental setup. See Appendix B, Fig. 5 for an image of the setup

$$g_{eff} = g_{L_2} m_{J_2} - g_{L_1} m_{J_1} \quad (7)$$

The energy difference E is the energy of the emitted photon, and can be translated into a wavenumber using $\Delta\nu = E/hc$. Using equation (6) we obtain the theoretical value of the splitting caused by the Zeeman effect, as a linear function of the magnetic field:

$$\Delta\nu = \frac{g_{eff}\mu_B}{hc} B \quad (8)$$

2.2 Apparatus

To verify the aforementioned theory, we aimed to measure the splitting of the emission lines caused by the external magnetic field in the hyper-fine structure. In order to achieve this, we employed the use of a Fabry-Perot interferometer that would enable us to measure the small differences in wavenumber between the split components of the line.

The experimental setup (Fig. 2) was comprised of the light source (Cd or Hg lamp), placed in between two electromagnets with iron cores. A filter selected the desired spectral line. A lens ($f = 10$ cm) created a parallel beam together with the iris that reduced the effective surface of the Fabry-Perot, potentially increasing resolution. An optical diffuser helped obtain a more uniform illumination, making measurements easier to perform. The Fabry-Perot interferometer and polariser are used to determine the type of polarisation observed and to select between different polarisations. The waveplate helped us determine the handedness of the circularly polarised light. The phenomenon is observed using a camera with focal length of $f = 75$ mm. The iris, diffuser, waveplate and polariser were used as required, in order to get the best image possible.

The plates of the Fabry-Perot can be adjusted with two piezoelectric crystals (on the two axes). We could find the position where the plates of the interferometer are parallel by moving the observer in the left-right and up-down directions and checking if the interference pattern changes. We started with the lens such that the light bulb is in focus, but later in the experiment we also tried moving it to obtain a more diffuse image of the bulb. This helped with the visibility of the interference ring. The camera focus was set to ∞ and the aperture was open all the way to maximise the light hitting the sensor.

The optical path $nd = 4.42 \pm 0.17$ mm between the plates of the Fabry-Perot was measured using the pattern observed for the red line ($\lambda = 644$ nm) and using the formula (9), where r_m is the radius of the m^{th} order and f_c is the focal distance of the camera (see section 3.1). We assumed that the refractive index does not significantly change as function of wavelength over the range tested. The interferometer needed to be re-calibrated after every set of measurements in order to keep the resolution as high as possible. This was probably caused by thermal expansion caused by the heating of the piezoelectric components.

$$nd = \lambda \frac{f_c^2}{r_m^2 - r_{m-1}^2} \quad (9)$$

The current in the electromagnets was correlated with the magnetic field obtained. We used a Hall effect sensor to measure the magnetic field in which the lamp will be placed. We used several readings at different currents to obtain the relation between the current in the coils and the field obtained (Fig. 6). For each current value we were able to measure a range of magnetic field values, because the field in between the two cores was not perfectly uniform. We tried to measure the value at the centre point and we estimated the error on the measurement based on how much the field changed as we moved the Hall effect probe in between the two iron cores. The fact that the field was not linear contributed to the widening of the observed lines. It was also observed that there was a residual magnetic field, because of the iron cores. This was accounted for when fitting the measurements. We were able to obtain a stronger field with the hollow iron cores (Fig. 6b) because the cores were mounted around 30% closer together.

The scale on the polariser (ranging from 0 to 360 degrees) was correlated with the direction of E-field using Brewster's angle. Vertical polarisation corresponds to 135 degrees (and horizontal at a 45° angle). We used the calibrated polariser to identify the polarisation of the lines under perpendicular observation. We identified the σ component as the one with polarisation perpendicular to the B field and the π component as polarised longitudinally. The order (and position) of the split σ and π components is as predicted by the Zeeman effect. Under longitudinal observation we were not able to observe π components (as predicted), and we were able to find that the σ components have circular polarisation. The handedness of the circular polarisation was determined in section 3.3 by using a 543nm quarter-wave plate.

2.3 Instrumental resolution

There are four main factors that limit the maximum wavenumber measurement resolution that can be obtained: Doppler broadening (a), Airy distribution (b), the non-uniformity of the B-field (c) and the mirror flatness (d).

- (a) The spectral width of a line will be dominated by Doppler broadening. By assuming a Boltzmann distribution $f(v) = \sqrt{\frac{m}{2\pi kT}} e^{-\frac{mv^2}{2kT}}$ for the particles, and by substituting the velocity v from the Doppler shift equation $f = f_0(1 + v/c)$, we were able to recognise a Gaussian distribution with the FWHM of:

$$\delta\nu_{\text{Dopp}} = \sqrt{\frac{8kT \ln 2}{mc^2}} \nu_0 \quad (10)$$

where m is the mass of an atom, T is the temperature and ν_0 is the wavenumber of the peak of the distribution. By introducing the temperature of $T = 500\text{K}$ into the equation, which is in line with the literature [JF36], we obtained an expected broadening in the range of:

$$\delta\nu_{\text{Dopp Cd red}} = 2.4\text{m}^{-1} \quad (11)$$

$$\delta\nu_{\text{Dopp Hg blue}} = 3.5\text{m}^{-1} \quad (12)$$

- (b) In theory, the resolution of a Fabry-Perot interferometer is related to the finesse F of the instrument by:

$$\delta\nu_{\text{instr}} = \Delta\nu_{\text{FSR}} F^{-1} = \frac{1}{2d} F^{-1} \quad (13)$$

where $\Delta\nu_{\text{FSR}}$ is the free spectral range of the instrument. According to [JHS96] we are expecting the reflectance of the mirrors of the Fabry-Perot to be $R = 0.95$. This is close enough to 1 to approximate the finesse to be given by equation (14).

$$F = \frac{\pi R^{\frac{1}{2}}}{1 - R} \quad (14)$$

This results in a theoretical maximum instrumental resolution limit of:

$$\delta\nu_{\text{instr}} = 1.6\text{m}^{-1} \quad (15)$$

- (c) The magnetic field in the space between the iron cores was not perfectly uniform: edge effects make the field lines diverge and the field weaker at the centre of the gap between the cores. We were able to measure the variation of the magnetic field with the Gauss meter (Fig. 6) and it is of the order of 5mT for the highest magnetic fields achievable with this setup. We estimated the broadening resulting from the Zeeman effect caused by a spectrum of B-fields using equation (8) to be at most:

$$\delta\nu_B = 0.5\text{m}^{-1} \quad (16)$$

This value corresponds to a $g_{eff} = \pm 2$ value, and because it is much smaller than the other sources of line broadening, it will not significantly contribute to the final total resolution limit of the instrument.

- (d) The flatness of the mirrors is essential in obtaining a sharp image, as a deviation of just $\lambda/2 \approx 250\text{nm}$ creates destructive interference. This is why we re-calibrated the mirror alignment after every set of measurements. Since we used a mirror surface with a dimension on the order of 1cm, any curvature with a radius lower than $R \approx 400\text{m}$ will make measurements impossible. We were not able to estimate the flatness of the mirror, but results (section 3.7) indicated this plays an important role in determining the total instrumental resolution limit (equation (17)).

The resulting total resolution limit of the instrument was estimated by adding in quadrature the individual errors, and is predicted to be at most:

$$\delta\nu_{\text{total}} = \sqrt{\delta\nu_{\text{Dopp}}^2 + \delta\nu_{\text{instr}}^2 + \delta\nu_B^2} = 3.9\text{m}^{-1} \quad (17)$$

2.4 Measurement

The fundamental equation that predicts the angular position of the maxima in a Fabry-Perot interferometer is:

$$m = 2\nu nd \cos \theta \approx 2\nu nd(1 - \theta^2/2) \approx 2\nu nd(1 - \frac{r_m^2}{2f_c^2}) \quad (18)$$

where m is the interference order and $\theta \approx r_m/f_c$ is the angle. By subtracting equations (18) for orders m and $m + 1$ we find that:

$$r_m^2 - r_{m+1}^2 = f_c^2/\nu nd \quad (19)$$

Equation (18) for a different component $\nu + \Delta\nu$ is:

$$m = 2(\nu + \Delta\nu)nd(1 - \frac{r_m'^2}{2f_c^2}) \quad (20)$$

Combining these equations we find the splitting $\Delta\nu$ to be:

$$\Delta\nu = -\frac{1}{2nd} \frac{r_m^2 - r_m'^2}{r_m^2 - r_{m+1}^2} \quad (21)$$

where r_m is the radius of the inner component, r'_m is the radius of the outer component for the order m , and nd is the optical path (9). The radii of the rings in the interference pattern are measured using the Thor Labs software (Fig. 7). The software is used to control shutter and gain of the camera to obtain the desired image brightness. We used the circular measure tool to manually fit circles to the maxima in the interference pattern and the software provides the radius of the circles in number of pixels.

3 Results

3.1 Interferometer plate separation measurement

We began our experiment by measuring the distance d between the plates of the interferometer as described in Section 2.2 obtaining:

$$d = 4.42 \pm 0.17\text{mm} \quad (22)$$

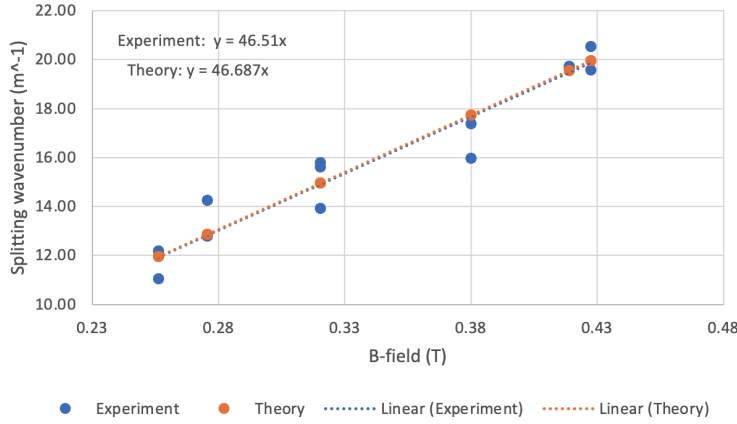


Figure 3: Line splitting for the σ polarised line due to the Zeeman effect in the cadmium red transition, $5^1D_2 \rightarrow 5^1P_1$, $\lambda = 643.85\text{nm}$

Despite changing the position of the plates when re-calibrating the interferometer in order to maintain the sharp image, we were not able to measure a change in the distance between the plates. This is because our error on distance d is on the order of 0.17mm and the adjustments made during re-calibration are much smaller than the error margin, on the order of the wavelength $\lambda \approx 500\text{nm}$. We conclude therefore that one should not be concerned with remeasuring the distance between the plates. It can also be safely assumed that the refractive index for air stays constant ($n = 1$), as its dependence on temperature and wavelength is much smaller than other sources of error in the experiment [Pol24].

3.2 Cadmium red transition - normal Zeeman effect

We first studied the $5^1D_2 \rightarrow 5^1P_1$ transition for the cadmium red line. We used Table 4 and equation (7) to find the possible values for the effective g-factor to be $g_{eff} = -1, 0, 1$. This means that we expected the line to split into 3 components, with the splitting given by equation (8). The theoretical value of the linear line splitting $\Delta\nu$ as function of magnetic field B for $g_{eff} = \pm 1$ is:

$$\text{Theoretical value: } \frac{\Delta\nu}{B} = 46.7 \text{ m}^{-1} \text{ T}^{-1} \quad (23)$$

We were able to observe that, as the magnetic field strength is increased, the maxima split into 3 components: the π component ($g_{eff} = 0$) remained in place and the two σ ($g_{eff} = \pm 1$) components moved apart on each side of the π line. The splitting was predicted to be symmetric between the ($g_{eff} = \pm 1$) pair, this was also experimentally confirmed. The magnitude of the splitting was plotted in Figure 3, with the linear dependence measured using a linear fit with 0 intercept (equation (24)).

$$\text{Measured value: } \frac{\Delta\nu}{B} = 46.5 \pm 3.6 \text{ m}^{-1} \text{ T}^{-1} \quad (24)$$

3.3 Electron charge to mass ratio

An interesting use of the experiment performed in section 3.2 is that we can employ the result (24) to derive the charge to mass ratio of the electron. The formula for the Bohr magneton $\mu_B = e\hbar/(2m_e)$ is introduced into equation (8), and after using that $g_{eff} = 1$ for this transition, we obtain:

$$\frac{e}{m_e} = 4\pi c \frac{\Delta\nu}{B} = (-1.75 \pm 0.14) \times 10^{11} \text{ C kg}^{-1} \quad (25)$$

This is in agreement with the theoretical value [NIS19]:

$$\frac{e}{m_e} = -1.75882001076(53) \times 10^{11} \text{ C kg}^{-1} \quad (26)$$

Interestingly, it is also possible to determine the sign of the electron charge. We used a beetle as reference for left hand polarised light. The beetle reflects bright green left-hand polarised light. Therefore we determined that the outer ring in the interference pattern were LH polarised and the inner ones were RH polarised. These measurements were done with a longitudinal setup, parallel to the magnetic field. We used a compass to determine that the B-field vector was in the direction of the photon momentum. Outer ring is higher energy ($\Delta\nu > 0$), and $\Delta m_J = 1$ corresponds to RH polarisation. By substitution into equation (8), this result confirms that electrons have negative charge.

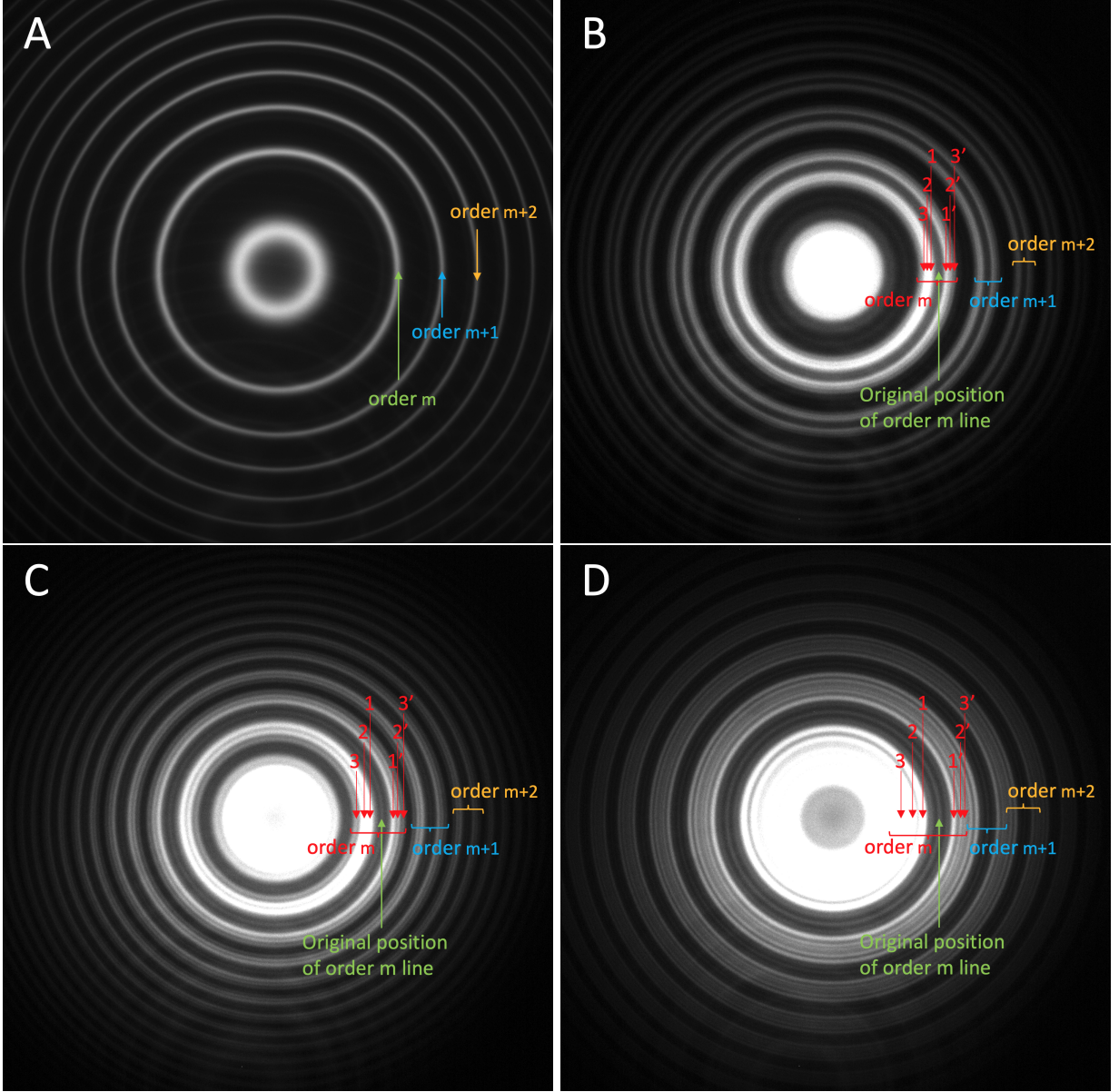


Figure 4: Fabry-Perot interferometer images of the cadmium green line observed along the field lines. Only the 6σ polarised lines are visible under longitudinal observation. Magnetic field is increased from 0.03T in Fig. A, to 0.46T in Fig. B, to 0.54T in Fig. C, and up to 0.62T in Fig. D. The lines are not resolved for field lower than in Fig B, and the different orders start overlapping for fields higher than in Fig D. The labels 3, 2, 1, 1', 2', 3' correspond to the $g_{eff} = -2, -1.5, -1, 1, 1.5, 2$ values respectively (see Table 1). The rings labelled with the primed number are referred to as outer rings and the non-primed are inner rings.

3.4 Cadmium green transition - anomalous Zeeman effect

The $5^3S_1 \rightarrow 5^3P_2$ transition, for the cadmium green line, exhibits the anomalous Zeeman effect: the spin of the electrons couple together and the interaction involves both the orbit and angular

momentum and the spin angular momentum. The anomalous Zeeman effect splits the spectral line in more than three components that are not necessarily equally spaced apart. The effective g-factor values, derived using Table 4 and equation (7) are shown in Table 1 together with their polarisation. Having 9 different possible values for g_{eff} means that we expect the line to split into 9 components, with the splitting given by equation (8).

| Observation configuration | Polarisation | g_{eff} | No. of independent measurements | Measured splitting $\Delta\nu/B$ ($m^{-1} T^{-1}$) | Theoretical splitting $\Delta\nu/B$ ($m^{-1} T^{-1}$) |
|---------------------------|--------------|-----------|---------------------------------|--|---|
| perpendicular | π | 0 | - | no splitting | 0 |
| perpendicular | π | ± 0.5 | 12 | 22.4 ± 1.0 | 23.4 |
| perpendicular | σ | ± 1 | 8 | 44.7 ± 2.1 | 46.7 |
| perpendicular | σ | ± 1.5 | 8 | 63.8 ± 2.9 | 70 |
| perpendicular | σ | ± 2 | 8 | 85.1 ± 3.9 | 93.4 |
| parallel | σ | ± 1 | 9 | 43.4 ± 2.0 | 46.7 |
| parallel | σ | ± 1.5 | 9 | 69.2 ± 3.3 | 70 |
| parallel | σ | ± 2 | 7 | 89.8 ± 4.1 | 93.4 |

Table 1: Cadmium green line: measured line splitting wavenumber $\Delta\nu$ dependence on magnetic field B and g_{eff} factor in the $5^3S_1 \rightarrow 5^3P_2$ transition. The calculated values of g_{eff} are shown with the corresponding polarisation according to the Zeeman effect predictions

This is indeed what we observed: when the magnetic field is applied, the line splits into 9 components. A polariser (or longitudinal observation) is used to select only the π or σ polarisations in order to more easily perform the measurements (see Fig. 4 with only σ polarisations). Our experiment verifies that the measured line splitting is the same in both longitudinal and perpendicular configurations.

3.5 Mercury green transition

The splitting of the mercury green line (Fig. 10, 11 and Table 2, transition $7^3S_1 \rightarrow 6^3P_2$) is the same as in the cadmium green (transition $5^3S_1 \rightarrow 5^3P_2$), within error, and in agreement with the theory. This confirms that the line splitting has no measurable dependence on the principal quantum number n or on other atomic properties of the material such as electron number Z .

| Observation configuration | Polarisation | g_{eff} | No. of independent measurements | Measured splitting $\Delta\nu/B$ ($m^{-1} T^{-1}$) | Theoretical splitting $\Delta\nu/B$ ($m^{-1} T^{-1}$) |
|---------------------------|--------------|-----------|---------------------------------|--|---|
| perpendicular | π | 0 | - | no splitting | 0 |
| perpendicular | π | ± 0.5 | 12 | 23.8 ± 1.4 | 23.4 |
| parallel | σ | ± 1 | 7 | 46.1 ± 2.0 | 46.7 |
| parallel | σ | ± 1.5 | 4 | 70.9 ± 3.0 | 70 |
| parallel | σ | ± 2 | 4 | 91.5 ± 4.1 | 93.4 |

Table 2: Mercury green line: measured line splitting wavenumber $\Delta\nu$ dependence on magnetic field B and g_{eff} factor in the $7^3S_1 \rightarrow 6^3P_2$ transition. The calculated values of g_{eff} are shown with the corresponding polarisation according to the Zeeman effect predictions

3.6 Mercury blue transition

The $7^3S_1 \rightarrow 6^3P_1$ transition is important because it proves the special case of the selection rule that predicts that for $\Delta J = 0$ there can be no transition where the quantum number m_j changes from 0 to 0. Therefore the observed interference pattern does not have the central π component corresponding to $g_{eff} = 0$. When we used a polariser to select only π polarised light, we observed only two components (Figure 15).

For the mercury blue transition there are 6 possible values for the g_{eff} coefficient (from equation (8)) as presented in Table 3. The absence of the central π component made possible measurements of the splitting of as low as $\Delta\nu = 8.7 \pm 0.3\text{m}^{-1}$ at magnetic fields of $B = 0.309 \pm 0.004\text{T}$.

| Observation configuration | Polarisation | g_{eff} | No. of independent measurements | Measured splitting $\Delta\nu/B$ ($\text{m}^{-1}\text{T}^{-1}$) | Theoretical splitting $\Delta\nu/B$ ($\text{m}^{-1}\text{T}^{-1}$) |
|---------------------------|--------------|-----------|---------------------------------|---|--|
| perpendicular | π | ± 0.5 | 16 | 25.6 ± 1.1 | 23.4 |
| parallel | σ | ± 1.5 | 1 | 74 ± 16 | 70 |
| parallel | σ | ± 2 | 1 | 90 ± 16 | 93.4 |

Table 3: Measured line splitting wavenumber $\Delta\nu$ dependence on magnetic field B and g_{eff} factor in the mercury blue $7^3S_1 \rightarrow 6^3P_2$ transition. The calculated values of g_{eff} are shown with the corresponding polarisation according to the Zeeman effect predictions

The measurements of the σ polarised components was highly limited by the resolution and free spectral range of the instrument used. The two σ pairs are located close together, at $|g_{eff}| = 1.5$ and $|g_{eff}| = 2$, making them unresolved for $B < 0.5\text{T}$. For $B > 0.5\text{T}$ the lines start overlapping with the next order, making measurements only possible at $B = 0.5\text{T}$. The values obtained are in agreement with the theory (Table 6), considering that one can use the FWHM $\delta\nu_{FWHM} = 8\text{m}^{-1}$ of the lines as an estimation of the order of magnitude of the error.

3.7 Interferometer resolution measurement

We directly measured the resolution of the Fabry-Perot setup by looking at the line profile of the interference image (See Fig. 17 and Fig. 18 in Appendix G). We define the resolution limit as the FWHM of the observed line measured in units of m^{-1} . We first measured the resolution limit of the instrument using the Hg lamp finding:

$$\delta\nu_{\text{Hg}} = 20.8 \pm 0.7\text{m}^{-1} \quad (27)$$

When investigating the cadmium green line (Fig 4A) we achieved a better resolution of $\delta\nu_{\text{Cd}} = 10 \pm 2\text{m}^{-1}$. This highlights how the setup is highly dependent on a good calibration. However, both of these values are a lot higher than the theoretically predicted resolution limit (equation 17). Equation (17) and (8) predicted that we should be been able to measure splittings for with $g_{eff} = \pm 1$ at as low a field as $B = 0.08\text{T}$. In practice we were only able to measure splittings for a minimum field of $B = 0.26\text{T}$ for the cadmium red line (fig. 3).

We also attempted to measure the inherent instrumental resolution by making use of a He-Ne laser, which does not have Doppler broadening. The laser light line width was measured using a Czerny-Turner monochromator and determined to be $\lambda_{\text{He-Ne}} = 633.1 \pm 0.4\text{nm}$. We measured the FWHM of the peaks in the line profile (Fig. 18) of the Fabry-Perot interference image (Fig. 19) and obtained a resolution limit of:

$$\delta\nu_{\text{He-Ne no iris}} = 7.9 \pm 1\text{m}^{-1} \quad (28)$$

without using an iris and with an iris:

$$\delta\nu_{\text{He-Ne with iris}} = 5.2 \pm 1\text{m}^{-1} \quad (29)$$

This suggests that the flatness (d) of the mirror accounts for most of the error in our measurement. The low instrumental resolution will be dominant over the Doppler broadening (equation (11)).

4 Error analysis

The leading source of error on the splitting measurements was the 3.8% error on the measurement of the distance d between the plates. Another significant source of error was random error from the interference maxima radius measurement. We calculated this as standard deviation of the individual

measurements. There was also a 1% error on the correlation between field strength and current. As we only directly measured current, this error affected all splitting measurements. These errors were considered independent and the final result is linearly dependent on these parameters, therefore we combine the percentage errors by adding them in quadrature.

Numerical errors were considered, but they turn out to be insignificant: In equation (18) it was assumed that θ is small (30), and θ^3 order and higher terms were neglected ($\theta^3 \approx 10^{-4}$).

$$\theta \approx \frac{\# \text{ of pixels} \times \text{pixel width}}{\text{focal distance}} \approx \frac{700 \times 5.86\mu\text{m}}{75\text{mm}} \approx 0.05 \ll 1 \quad (30)$$

5 Conclusions

5.1 Further work

To enhance the experiment's efficacy, future iterations could incorporate a Fabry-Perot interferometer with higher resolution, facilitating the measurement of splittings at lower field strengths. Employing alternative light sources may be necessary to mitigate Doppler broadening, a primary limiting factor. Moreover, utilising a current source and electromagnet combination capable of generating stronger magnetic fields together with a Fabry-Perot interferometer with a higher free spectral range would enable measurements with stronger fields, up to the point where the Zeeman effect model starts to break down and one needs to use the Paschen-Back Effect to describe the phenomenon. Future study could enable applications such as more precise control of atomic and molecular properties for advancements in fields like quantum computing.

5.2 Aims and results

This experimental investigation aimed to validate theoretical predictions regarding the Zeeman effect through the observation of spectral line splittings in the presence of magnetic fields in transitions of cadmium and mercury. Each of the following transitions verify a property of the phenomenon:

- $5^1D_2 \rightarrow 5^1P_1$: the normal Zeeman effect (spin 0 case) follows semi-classical prediction
- $5^3S_1 \rightarrow 5^3P_2$: the anomalous Zeeman effect has spin dependence
- $7^3S_1 \rightarrow 6^3P_1$: for $\Delta J = 0$ there is no transition where m_j changes from 0 to 0
- $7^3S_1 \rightarrow 6^3P_2$: the splitting does not depend on the quantum number n

Our experiment measured the polarisations of the line components and confirmed that we obtain π polarisation for $\Delta m_j = 0$ and σ polarisation for $\Delta m_j = \pm 1$. Under transverse observation relative to the magnetic field the π and σ lines are linearly polarised parallel and perpendicular to the B-field respectively. Under longitudinal observation π lines are missing and σ lines are circularly polarised. We measured the handedness of the polarisation to be left-handed for $\Delta m_j = -1$ and right-handed for $\Delta m_j = 1$.

We derived the electron charge to mass ratio from the ratio of the splitting to the magnetic field strength. We also determined the sign of the electron charge using the handedness of the circularly polarised light observed. Additionally, we investigated the resolution of the Fabry-Perot using a He-Ne laser as a monochromatic light source.

References

- [BS15] James Binney and David Skinner. *8.2*, page 236–274. Oxford Univ. Press, 2015.
- [Foo05] C. J. Foot. *Atomic Physics*. Oxford University Press, Incorporated, 2005.
- [JF36] C. V. Jackson and Alfred Fowler. The red line of cadmium as a standard of wave-length. *Proceedings of the Royal Society of London. Series A - Mathematical and Physical Sciences*, 155(885):407–419, 1936.

- [JHS96] JHS. AD21 A guide to the Fabry-Perot etalon. https://www-teaching.physics.ox.ac.uk/practical_course/Admin/AD21.pdf, 1996. Revised October 2021.
- [NIS19] NIST. 2018 CODATA Value: electron charge to mass quotient, 2019. Retrieved 2024-01-22.
- [Pol24] Mikhail N. Polyanskiy. Refractiveindex.info database of optical constants. *Scientific Data*, 11(1):94, 2024.

A Appendix - Energy levels and allowed transitions

| State | L | S | J | m_J |
|----------|---|---|---|-----------------|
| 5^1D_2 | 2 | 0 | 2 | -2, -1, 0, 1, 2 |
| 5^1P_1 | 1 | 0 | 1 | -1, 0, 1 |
| 5^3S_1 | 0 | 1 | 1 | -1, 0, 1 |
| 5^3P_2 | 1 | 1 | 2 | -2, -1, 0, 1, 2 |
| 7^3S_1 | 0 | 1 | 1 | -1, 0, 1 |
| 6^3P_1 | 1 | 1 | 1 | -1, 0, 1 |
| 7^3S_1 | 0 | 1 | 1 | -1, 0, 1 |
| 6^3P_2 | 1 | 1 | 2 | -2, -1, 0, 1, 2 |

Table 4: The corresponding possible quantum numbers for the states reached by the transitions studied.

The quantum mechanical analysis of the transitions predicts the following selection rules for electric dipole transitions (Table 5):

| Selection Rule | Description |
|---|------------------------------------|
| $\Delta J = 0, \pm 1$, but not $0 \rightarrow 0$ | Change in total angular momentum |
| $\Delta M_J = 0, \pm 1$, but not $0 \rightarrow 0$ if $\Delta J = 0$ | Change in magnetic quantum number |
| $\Delta L = \pm 1$ | Change in orbital angular momentum |
| $\Delta S = 0$ | No change in spin |

Table 5: Selection rules for electric dipole transitions

B Appendix - Experimental setup



Figure 5: Experimental setup in the parallel observation configuration, iris not included. See schematic illustration if Fig. 2

C Current to field conversion

D User interface

The user interface used to make measurements is shown in figure 3. We used the circle tool to overlay circles on the interference maxima. The circle radius is measured in pixels and then converted to

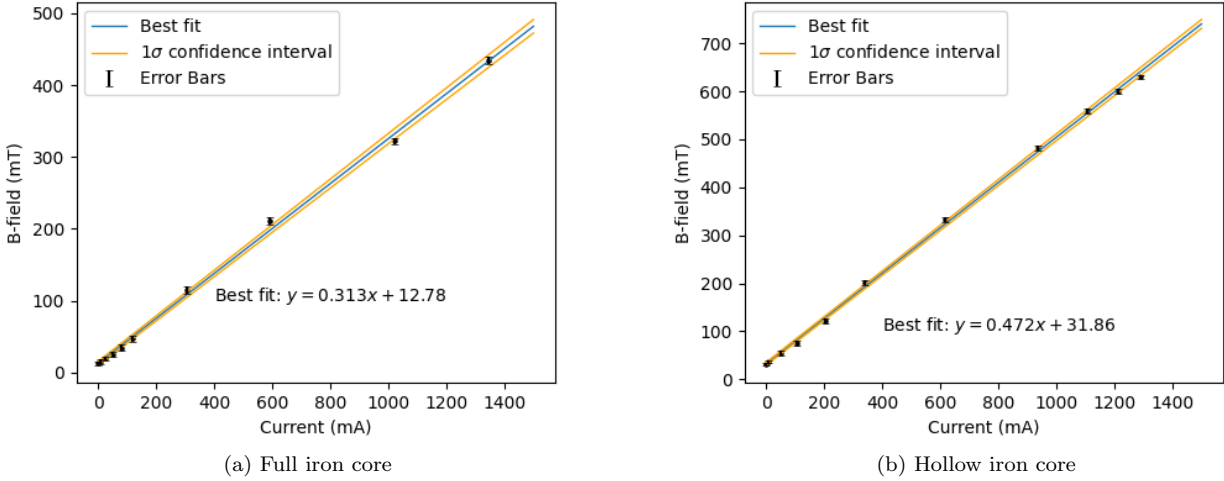


Figure 6: Conversion of the applied current to magnetic field. The data was fitted with a linear fit ($y = ax + b$) using the method of least squares. Data points shown as central value \pm variation of the field in the gap between the cores. Parameters of the best-fit are: 6a: $a = 0.312 \pm 0.004 \text{ T A}^{-1}$ and $b = 0.013 \pm 0.002 \text{ T}$ and 6b: $a = 0.472 \pm 0.004 \text{ T A}^{-1}$ and $b = 0.032 \pm 0.003 \text{ T}$

milimiters using the known size of pixels.

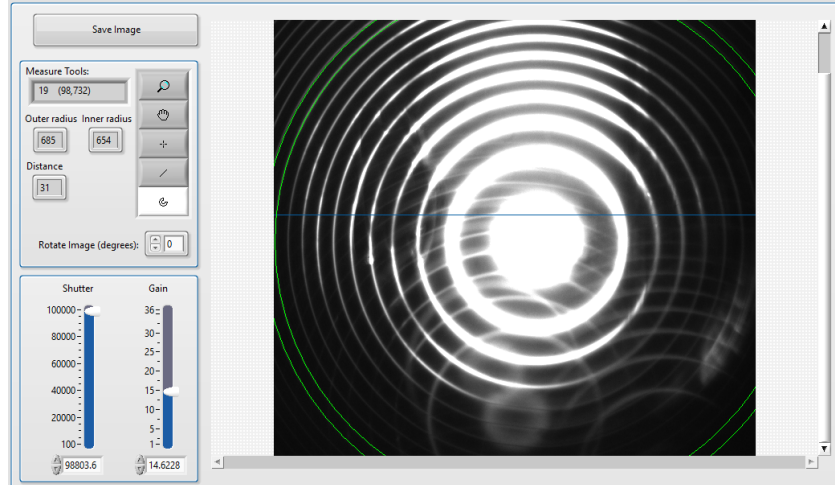


Figure 7: User interface of the program used for measurements. Image shows the Fabry-Perot interference pattern of the cadmium red line, no magnetic field applied.

E Appendix - Splitting measurements plotted

E.1 Cadmium

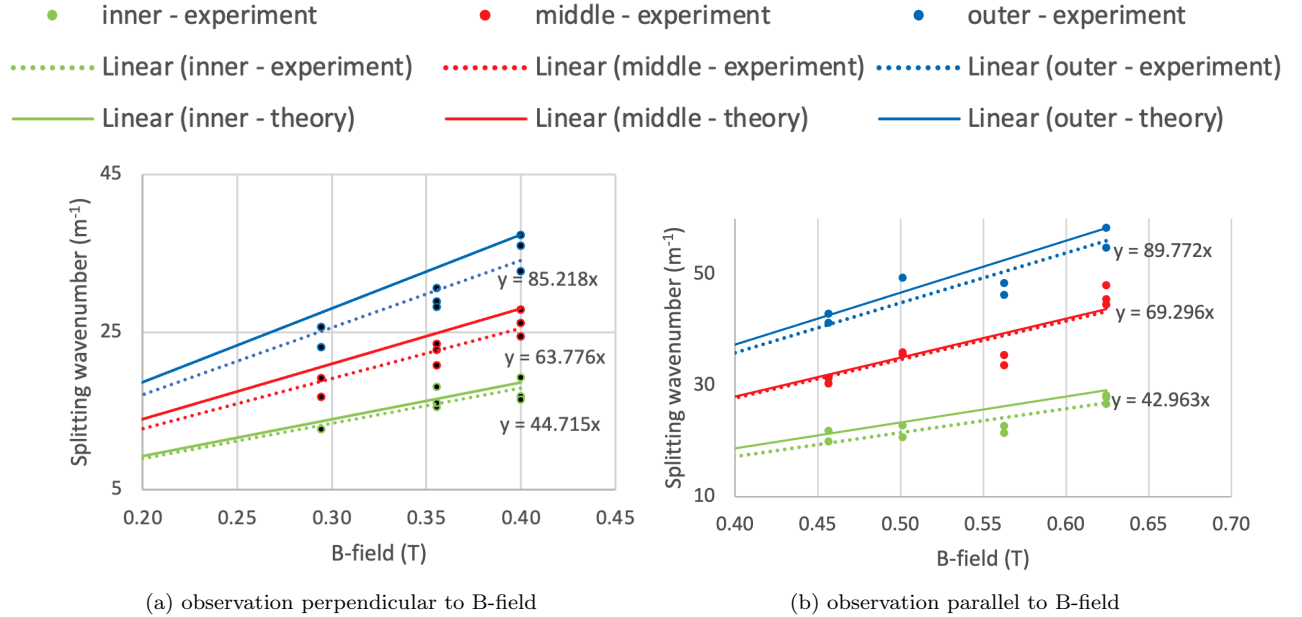


Figure 8: Line splitting due to Zeeman effect in the σ polarised lines in the cadmium green line. "inner", "middle" and "outer" data correspond to the pairs of lines labelled (1, 1'), (2, 2') and (3, 3') in Fig. 4. We used a linear fit with intercept of 0 to fit the data. Theoretical dependence is shown with a solid line.

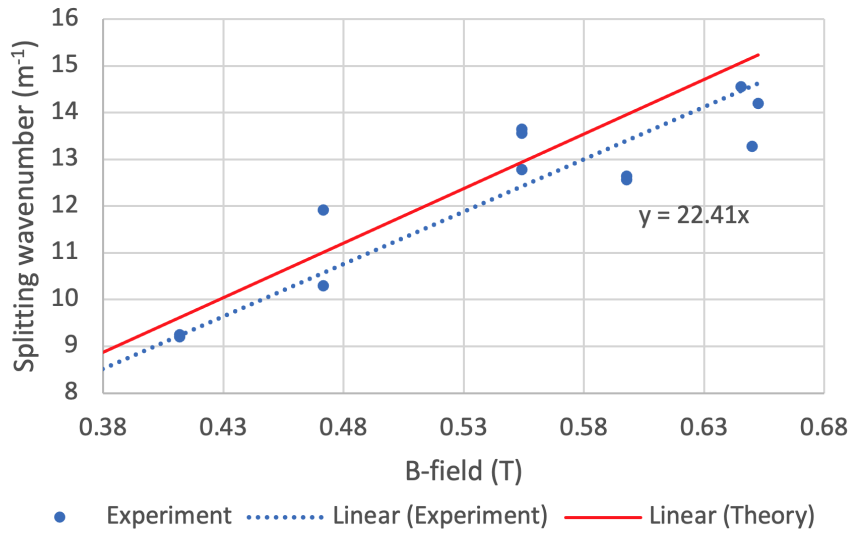


Figure 9: Line splitting due to Zeeman effect in the π polarised lines in the cadmium green line with the perpendicular configuration

E.2 Mercury

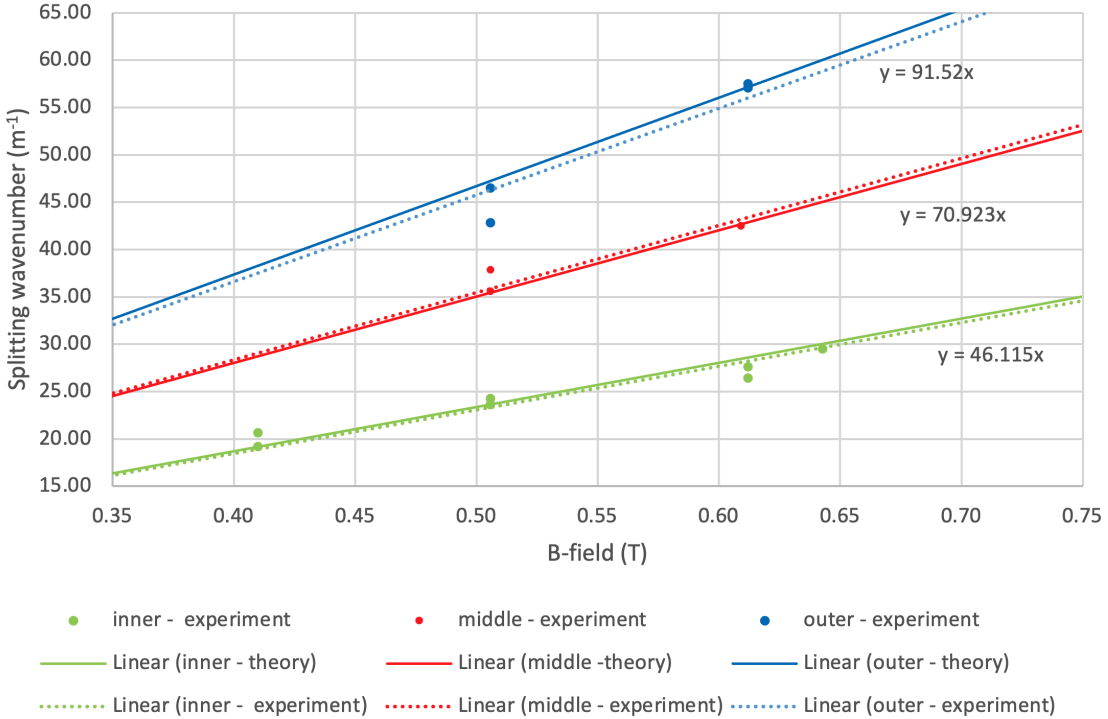


Figure 10: Line splitting due to Zeeman effect in the σ polarised lines in the mercury green line with the parallel configuration. The dotted lines are the linear fits of the measurements, the solid lines are theoretical predictions. Inner, middle and outer components are shown in green, red and blue and correspond to the $(1, 1')$, $(2, 2')$ and $(3, 3')$ pairs respectively (see Fig. 4)

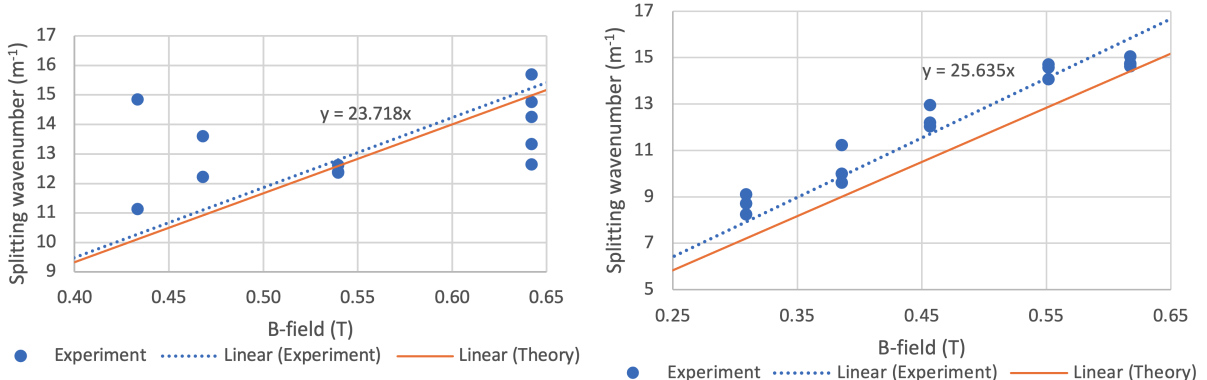


Figure 11: Line splitting due to Zeeman effect in the π polarised lines in the mercury green line with the perpendicular configuration

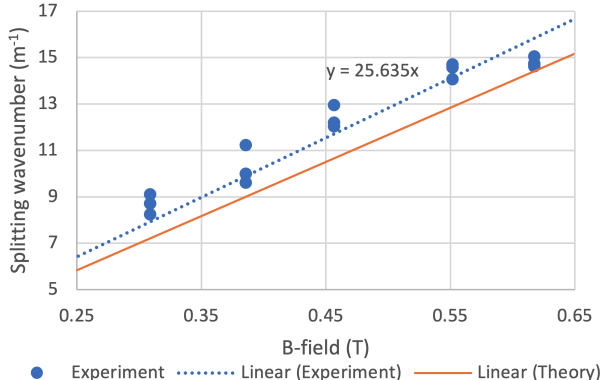


Figure 12: Line splitting due to Zeeman effect in the π polarised lines in the mercury blue line with the perpendicular configuration

| g_{eff} | B-field T | Measured $\Delta\nu \pm \text{FWHM}(\text{m}^{-1})$ | Theoretical $\Delta\nu (\text{m}^{-1})$ |
|-----------|-----------|---|---|
| ± 1.5 | 0.5 | 36.8 ± 8 | 35.28 |
| ± 2 | 0.5 | 44.97 ± 8 | 47.04 |

Table 6: Measurements of the line splitting $\Delta\nu$ in the mercury blue sigma lines

F Appendix - Fabry-Perot images

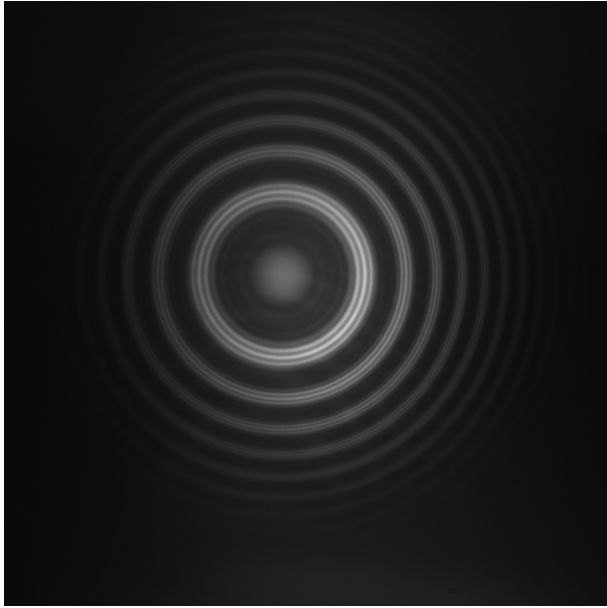


Figure 13: Fabry-Perot interferometer image of the cadmium green line with magnetic field applied in the perpendicular configuration. Only π lines visible

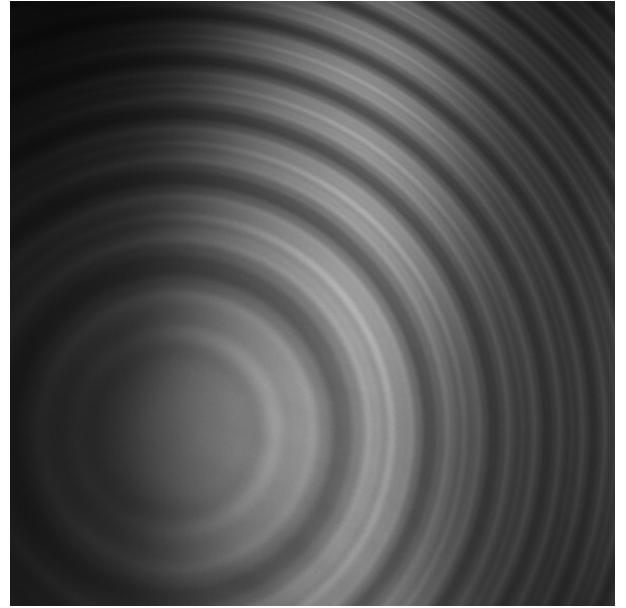


Figure 14: Cropped Fabry-Perot interferometer image of the mercury green line with magnetic field applied in the perpendicular configuration. All 9 split components are visible. The outer components have low relative intensity and the split components fill the full spectral range of the interferometer, therefore it might be hard to identify all components without adjusting the magnetic field.

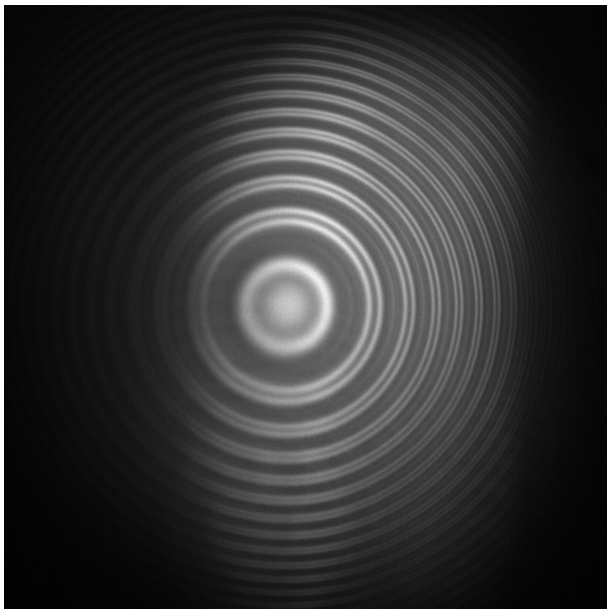


Figure 15: Fabry-Perot interferometer image of the mercury blue line with magnetic field applied in the perpendicular configuration. Only π lines visible

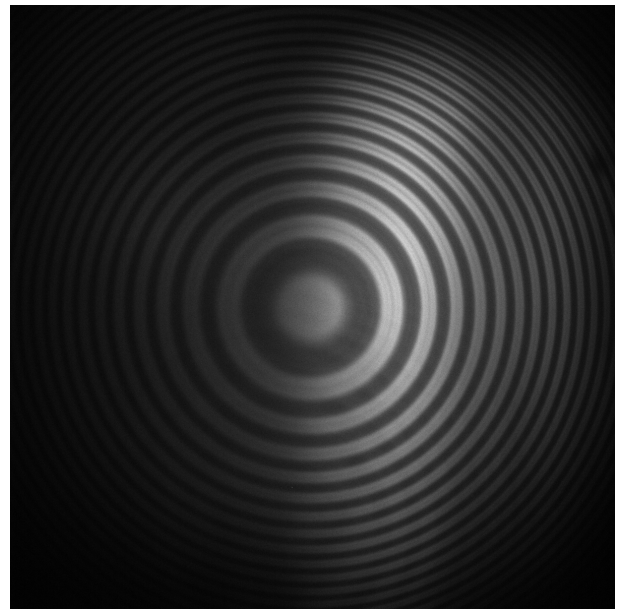


Figure 16: Fabry-Perot interferometer image of the mercury blue line with magnetic field applied. Only σ lines visible

G Appendix - Line profiles of the instrument

The experiment investigated the line profiles of the instrument (section 3.7) in order to characterise the resolution of the Fabry-Perot interferometer and determine the leading source of uncertainty. Line profiles were plotted using the mercury light (Fig. 17) and using a Helium-Neon laser with a much narrower inherent line width. The laser light also had a much narrower beam, reducing the importance of having an interferometer with perfectly flat plates. Both of these facts reduced the FWHM observed (Fig. 18 and 19).

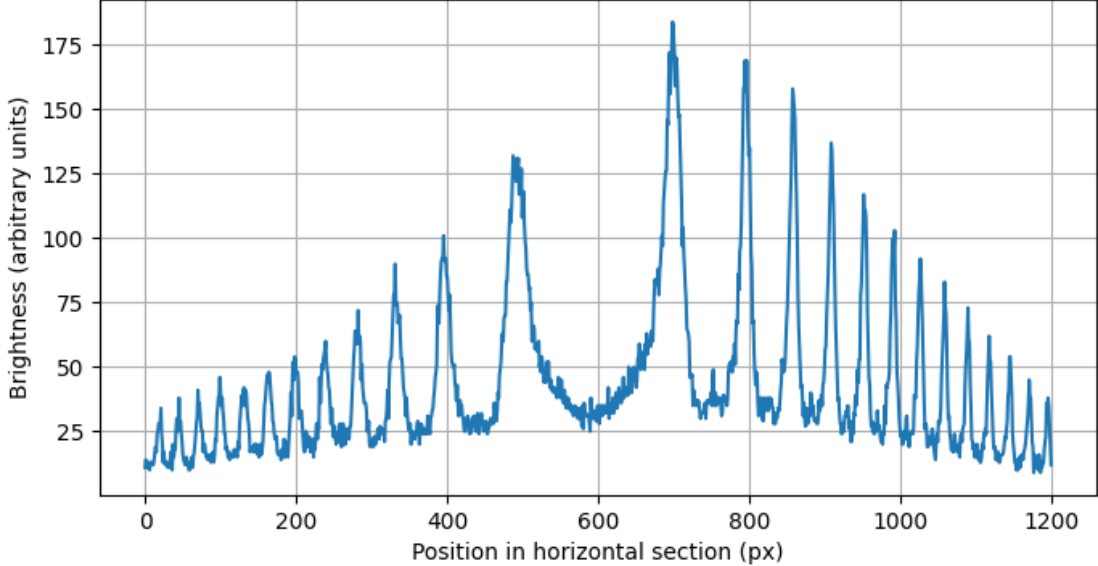


Figure 17: Horizontal line profile through the centre of the Fabry-Perot interference pattern produced by the mercury blue line with no external magnetic field applied

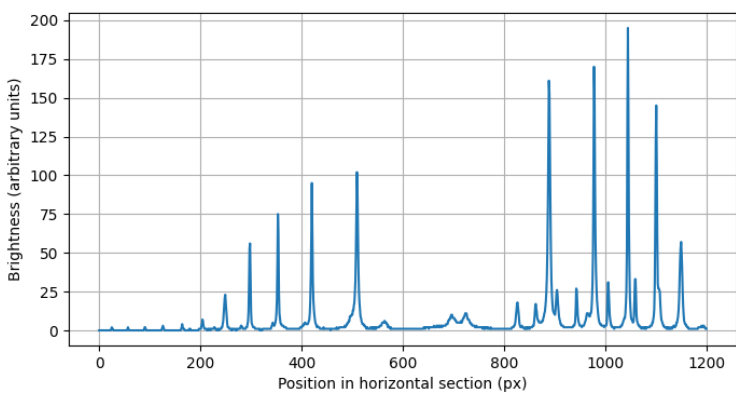


Figure 18: Horizontal line profile through the centre of the Fabry-Perot interference pattern produced by the He-Ne laser



Figure 19: Fabry-Perot interference pattern produced by the He-Ne laser